

Simulating urban heat island for predicting its spatial pattern in meso level town of India

Sk Ziaul, Swades Pal *

Dept. of Geography, University of Gour Banga, Mokdumpur, Malda 732103, West Bengal, India



ARTICLE INFO

Keywords:

Artificial neural network
Land surface temperature
Landscape indices
Hot and cold spots
Spatial autocorrelation
FRAGSTATS

ABSTRACT

The increase in urban land surface temperature (LST) has become an environmental challenge to urban dwellers and policymakers. To adopt mitigation plans, prediction, and pattern recognition of future temperature is very essential approaches. Therefore this present study intended to simulate future LST patterns using artificial neural networks (ANN) and recognize its spatio-temporal pattern using three different approaches such as hot and cold spot analysis, spatial autocorrelation, and fragmentation analysis. Simulation results show that the area under a comparatively higher temperature intensity zone is predicted to be increased over time. For example, in April month, 1709.73 ha area of $>32.34^{\circ}\text{C}$ temperature zone in 2017 is predicted to be enlarged by 4079.97 ha in 2037. Accordingly, the results of pattern recognition reveal that area under significant cold spot of winter season decreased from 1046.24 ha in 2007 to 961.07 ha in 2027 and predicted to further decrease as 794.25 ha and 302 ha in 2027 and 2037 respectively. Similarly, very high spatial adjacency of LST with high Morain's I values (0.74–0.99) has been found both in actual and predicted years in summer season. Besides, the large core of uncomfortable low temperature fragmented into medium and small core over time while opposite result has been found in case of uncomfortable high temperature.

1. Introduction

Accelerating urban growth is considered as responsible factor for several environmental and social problems around the world. One of the main ramifications of rapid urban growth is transformation of natural land to impervious surface. Such alteration of land surface bring a variation in moisture content of soil, heat retention capacity, albedo as well as surface emissivity etc. (Chudnovsky et al., 2004; Friedl, 2002). Another serious environmental outcome of speedy urban growth is ascending of land surface temperature (LST) and air temperature in urban area than its proximate rural area and such occurrence in urban area is known as urban heat island (UHI) (Chakraborty et al., 2017; Rizwan et al., 2008). Several researchers (McCarthy et al., 2010; Zhang et al., 2013; Seto et al., 2012) have reported that due to the rapid urban growth, urban thermal environment is anticipated to be change with growing the urban population globally. Furthermore, UHI have so many adverse effects such as human health related problem (Mohan and Kandya, 2015; Goggins et al., 2012), cause of high amount of water and energy consumption (Akbari et al., 2016) and bring the changes in land surface phenology (Zipper et al., 2016). Therefore UHI studies has becomes a huge area of interest to the policy maker as well as scientific experts for its benefaction to different fields specifically climatology, atmospheric environment (Luo and Lau, 2017; Sun et al., 2016; Zhou et al. (2017)). Thus estimation of UHI intensity becomes very essential task in making plans and policies of sustainable

* Corresponding author.

E-mail address: swadeshpal82@gmail.com (S. Pal).

urban growth. Recently, computation and monitoring of UHI has become facilitated because of thermal satellite data. A number of studies have been carried out on land use land cover (LULC) change and its consequences on LST using satellite data (Li et al., 2009; Xu et al., 2013; Patz et al., 2005; Yuan and Bauer, 2007). Among the preceding works in this field, almost in all the studies, scholars have emphasized on the temporal transformation of LULC and their dominance on LST focusing less important on prediction as well as simulation of LST pattern (Odindi et al., 2015; Weng et al., 2004; Valsson and Bharat, 2009). The several simulation tools and techniques are obtainable for the predictions of oncoming LULC change of a particular area and these techniques can also be used to simulate the future LST of that area on the basis of relevant regulating factors. Moreover, it was reported by several scholars (Chen et al., 2006; Deng and Wu, 2013; Li and Liu, 2008; Yuan and Bauer, 2007) that there is profound relationship between LST and various land cover indices. Therefore on the basis of these significantly correlated land cover indices such as normalized difference built up index (NDBI) and vegetation fraction (FVG), the ulterior surface temperature can be predict with high precision. However, despite having significant correlation between LST and indices of different land cover, very few researches have applied indices of land surface parameters in prediction of future distributional pattern of LST. Hasanlou and Mostofi (2015) applied couple of land cover indices such as Normalized Difference Vegetation Index (NDVI), NDBI, Normalized Difference Water Index (NDWI), Normalized Difference Bareness Index (NDBal), Enhanced Built-up and Bareness Index (EBBI) etc. to estimate the LST. Besides Ahmed et al. (2013) and Mushore et al. (2017) computed future land surface temperature pattern on the basis of land surface parameters.

Markov Chain, Cellular Automata and Logistic Regression are very repeatedly applied simulation methods. In prior studies, all most in all the cases, global and regional models have been used to simulate temperature considering impact of urban trends as negligible standard (McCarthy et al., 2010; Unganai, 1996; Saitoh et al., 1996). Among all these simulation methods, ANN becomes a compatible method for simulation for its efficiency in prediction of future trend without knowing prior consciousness about the in real world

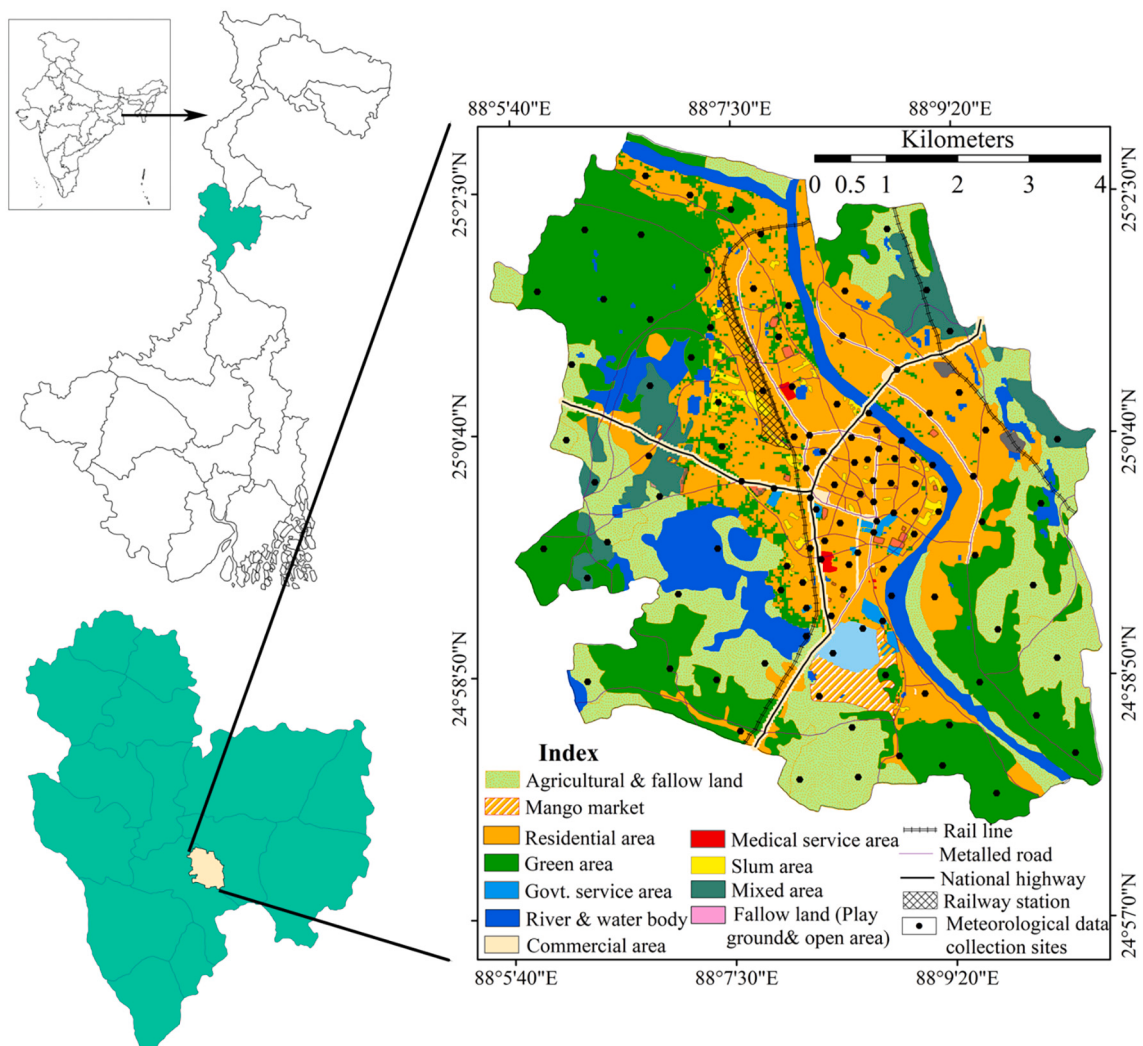


Fig. 1. Location of English Bazar Municipality and its surrounding suburban area showing meteorological data collection sites over different urban morphological units.

complex. Several scholars (Alsarraf et al., 2020; Choubin et al., 2020; Le et al., 2019; Liu et al., 2020) opted ANN for spatial as well as numerical simulation. Moreover, ANN can discern perplexing datasets introducing significant problems of statistical techniques on account of its nonlinear structure. Therefore, ANN is considered as best method to simulate the time series system.

Like future simulation and prediction of LST, identification of thermally consistence hot and cold spot as well as pattern recognition is very effective measures to adopt mitigation strategies. In this context, satellite imagery data specifically the thermal infrared (TIR) data can be the most compatible tool to delineate thermal hot spot and cold spot and identify the correlation between thermal environment and land use land cover (LULC) composition. However, hot and cold spot refers that area where the higher and lower LST exists respectively compared to their proximate area. One of the largely used method for analyzing the clustering pattern of hot spot and cold spot is The Getis-Ord Gi* method. In several studies, this method has been applied in various way e.g. in disaster management studies (Agathangelidis et al., 2016), in recognition of urbanization pattern (Chen et al., 1983), healthcare studies (Tsai et al., 2009), infrastructure development studies (Rauner et al., 2016), in transport management studies (Yun et al., 2016), green volume estimation (Handayani et al., 2018) incident management (Songchitruksa and Zeng, 2010), in assessment of heat wave vulnerability (Wolf and McGregor, 2013), and in identification of LST changing pattern (Li et al., 2016a, 2016b; Majumdar and Biswas, 2016). Besides this, the identification of hot spot and cold spot with high resolution satellite data (>30 m) (Coutts et al., 2016) may be helpful to collect the information regarding the spatial distribution of air temperature. Already several studies have been carried out on calculation of air temperature data using satellite imageries data (Chen et al., 1983; Gallo et al., 2011; Agathangelidis et al., 2016; Stathopoulou and Cartalis, 2009; Nichol et al., 2009). In this point of view, Landsat satellite imageries are the most compatible datasets to delineate hot spot and to support in adaptation of mitigation plans minimizing UHI effects just because of its good spatial coverage, freely accessibility.

The English Bazar Municipality, present study area is a *meso* level town, undergoing through compact population concentration along with vertical as well as horizontal urban growth (Dutta and Das, 2018a; Dutta and Das, 2019b). This meso level town covers 5465.43 ha area (100 ha = 1 km²) consisting both urban mainland and proximate suburban area (Fig. 1). Within this town, the decadal growth rate of population was recorded 24.78% and 21.5% in between 1991–2001 and 2001–2011 respectively. Since last 15 years, vertical growth of the town in terms of high rise residential and commercial buildings has been raised significantly to accommodate exceeding population. Pal and Ziaul (2017) reported that progressive concretization, the high rise of metallic infrastructure, traffic density, growing energy outlay, breaching of vegetated lands and water bodies are the dominant causes of increasing Urban heat island intensity (UHII) of this town. The four dominant seasons area found over the study area such as, (1) winter season consists of January and February months, (2) Pre monsoon or summer runs from March to May characterized with little rain and maximum temperature (>35 °C) and evaporation (3) Monsoon season runs from June to Mid-October having high temperatures and maximum rain (about 82% of total rain) and (4) Post-monsoon season runs from Mid-October to Mid-December. With impetuous urban growth and densification of urban area, the variation in thermal environment of this town seems to be a major concern to the urban dwellers.

Table 1

Details specification of Landsat imageries.

Sl. No.	Season	Date of capture	Sensor	Season	Date of capture	Sensor	Season	Date of capture	Sensor
1	Winter	17-12-88	TM	Summer	05-04-88	TM	Post Monsoon	15-11-88	TM
2		10-01-89	TM		08-04-89	TM		02-11-89	TM
3		05-01-90	TM		11-04-90	TM		20-10-90	TM
4		08-01-91	TM		30-04-91	TM		08-11-91	TM
5		27-01-92	TM		15-03-92	TM		13-11-92	TM
6		13-01-93	TM		03-04-93	TM		13-11-93	TM
7		18-12-94	TM		21-03-94	TM		15-10-94	TM
8		19-01-95	TM		25-04-95	TM		19-11-95	TM
9		22-01-96	TM		13-05-96	TM		05-11-96	TM
10		24-01-97	TM		30-04-97	TM		08-11-97	TM
11		12-02-98	TM		01-04-98	TM		Clouded	
12		14-01-99	TM		04-04-99	TM		Clouded	
13		17-01-00	TM		21-03-00	TM		31-10-00	TM
14		19-01-01	TM		25-04-01	TM		26-10-01	ETM
15		16-12-02	ETM		19-03-02	ETM		29-10-02	ETM
16		Clouded			22-03-03	ETM		25-11-03	ETM
17		29-12-04	TM		01-04-04	TM		11-11-04	TM
18		14-01-05	TM		19-03-05	TM		14-11-05	TM
19		25-01-06	TM		23-04-06	TM		17-11-06	TM
20		20-01-07	TM		10-04-07	TM		Clouded	
21		24-12-08	TM		28-04-08	TM		22-11-08	TM
22		09-01-09	TM		15-04-09	TM		09-11-09	TM
23		28-01-10	TM		Clouded			Clouded	
24		31-01-11	TM		21-04-11	TM		15-11-11	TM
25		Clouded			30-03-12	TM		Clouded	
26		Clouded			Clouded			20-11-13	OLI TRIS
27		Clouded			13-04-14	OLI TRIS		23-11-14	OLI TRIS
28		28-12-15	OLI TRIS		15-03-15	OLI TRIS		26-11-15	OLI TRIS
29		13-01-16	OLI TIRS		17-03-16	OLI TIRS		28-11-16	OLI TIRS
30		15-01-17	OLI TIRS		23-05-17	OLI TIRS		30-10-17	OLI TIRS

Besides, during summer season, about 82.41% area out of total study area falls under physiologically strong heat stress (Ziaul and Pal, 2019). If the present account is like this, what will be spatial pattern of LST as well as thermal comfortability in upcoming decades? Therefore considering this concerning issue, this present study intended to simulate and predict the LST of 2027 and 2037 both spatially and numerically in different seasons and analyze the temporal status of clustering pattern of hot spot and cold spot, fragmentation pattern of spatial high and low temperature zone and spatial adjacency.

2. Materials and methods

For the estimation of spatio-temporal LST since 1988 to 2017, Landsat satellite imageries of three different sensor such as Thematic Mapper (TM), Enhanced Thematic Mapper (ETM) and Thermal Infrared Sensor (TIRS) of 139/43 path/raw have been collected from the website of United State Geological Survey (USGS). The thermal bands (band 6 of TM/ETM, band 10 and 11 of TIRS sensor) were used to calculate LST. Resolution of these thermal bands is 120 m for TM, 60 m for ETM and 100 m for TIRS. MCP non-contact digital laser infrared thermometer (Y9-Y795-68 L6) was used to collect surface temperature data from 120 sites across the study area at same time (10 am) on which Landsat satellite captured the imagery. This data further used to validate the image based surface temperature model.

2.1. LST extraction

Land surface temperature has been computed using Landsat satellite imageries (Table 1). Thermal electromagnetic energy released by each and every object as its temperature is above absolute zero (K). According this principle, the signals captured by the thermal sensors (TM/ETM/TIRS) can be altered to at sensor radiance. Therefore the Eq. (1) (Landsat Project Science Office, 2002) is used to compute the spectral radiance (L_λ).

$$L_\lambda = \text{"gain"} + DN + \text{"bias"} \quad (1)$$

where, L_λ denote the spectral radiance of the thermal band of Landsat in $\text{W}/(\text{m}^2 \text{ sr } \mu\text{m})$, gain indicate the slope of the radiance/DN conversion function; DN refers the digital number of a given pixel; bias is the intercept of the radiance/DN conversion function. Eq. (1) can also be revealed as Eq. (2).

$$L_\lambda = \left(\frac{LMAX\lambda - LMIN\lambda}{QCALMAX - QCALMIN} \right) * (QCAL - QCALMIN) + LMIN\lambda \quad (2)$$

where, L_λ refer the Spectral radiance of the thermal band at sensor aperture in $\text{W}/(\text{m}^2 \text{ sr } \mu\text{m})$, $QCALMIN = 0$, $QCALMAX = 255$, $QCAL$ represent the quantized calibrated pixel value or DN value. The $LMAX$ and $LMIN$ denote the spectral at sensor radiance for band 6 at digital numbers 0 and 255 respectively.

2.1.1. Transformation of spectral radiance (L_λ) to At-satellite brightness temperatures (TB)

Spectral radiance of thermal bands of Landsat TM and TIRS respectively were changed to at satellite brightness temperature (TB) with the help of thermal calibration constants provided in metadata file. Therefore TB has been calculated using Eq. (3) (Landsat Project Science Office, 2002).

$$TB = \frac{K2}{\ln\left(\frac{K1}{L_\lambda} + 1\right)} \quad (3)$$

where, TB refers at-satellite brightness temperature (K), L_λ represents the spectral radiance of the thermal band at sensor aperture in $\text{W}/(\text{m}^2 \text{ sr } \mu\text{m})$, K_1 and K_2 represent the calibration constant in $\text{W}/(\text{m}^2 \text{ sr } \mu\text{m})$ (For Landsat-5 TM, $K_2 = 1260.56 \text{ W}/(\text{m}^2 \text{ sr } \mu\text{m})$, $K_1 = 607.76 \text{ W}/(\text{m}^2 \text{ sr } \mu\text{m})$ which are provided in metadata file.

2.1.1.1. Calculation of Land surface temperature (LST). The above obtained temperature values are referenced to a black body. Hence correction for spectral emissivity (ϵ) (Eq. 4) is essential to be done according to the nature of land cover (Snyder et al., 1998). These can also be carried out by attaining the corresponding values of emissivity from the proportion of vegetation (P_v) (Eq. 5) values for each pixel. The emissivity rectified land surface temperatures (S_t) were computed using the Eq. (6) (Artis and Carnahan, 1982).

$$\text{Land surface emissivity } (\epsilon) = 0.004 * P_v + 0.986 \quad (4)$$

where, proportion of vegetation (P_v) has been computed using the Eq. (5)

$$P_v = \left(\frac{NDVI_{j_r} - NDVI_{\min}}{NDVI_{\max} - NDVI_{\min}} \right)^2 \quad (5)$$

$$St = TB / [1 + \{(\lambda * TB / \rho) * \ln \epsilon\}] \quad (6)$$

where, S_t denote the land surface temperature (LST) in Kelvin, λ refer the wavelength of emitted radiance (for which the peak response and the average of the limiting wavelengths (Markham and Barker, 1985) is used), T_B represent at sensor brightness temperature (K), $\rho = h \times c/\sigma(1.438 \times 10^{-2} m \cdot K)$, σ is Boltzmann constant($6.626 \times 10^{-34} Js$), c is velocity of light ($2.998 \times 10^8 m/s$) and ϵ is emissivity (ranges between 0.97 and 0.99 (see Eq. (5)).

For better comprehension the above computed LSTs' unit was converted to degree Celsius using the relation of $0^\circ C$ equals 273.15 K.

After extracting LST of each year since 1988–2017 for each selected seasons, decadal average surface temperature has been computed.

2.1.2. Computation of decadal temperature gap

In order to calculate decadal temperature gap, all the study years since 1988 to 2017 have been categorized into three different phases such as phase 1 (1988–97), phase 2 (1998–07) and phase 3 (2008–17). After doing that, temperature of previous phase has been subtracted from present phase to find out the temperature gap in different phase.

2.2. Validation of LST

Validation of LST models have been done through estimating root means square error (RMSE) between images based LST and observed temperature data. In this regard, ground truth data has been collected through primary field survey at 150 sites using an infrared thermometer. On the basis of this data, RMSE has been calculated following Kuang et al. (2010). RMSE has been calculated for recent year (2017) based on ground truth data. Due to the scarcity of ground truth data of previous year, it is predicted that if the LST model of recent years is valid, model of previous will be considered as valid.

2.3. Simulating LST for future prediction

Cellular automata (CA) model using ANN (Jain et al., 1996) has been used to simulate and predict the future LST distributional pattern in MOLUSCE plugin of QGIS software environment. Recently, ANN is used frequently in different approaches such as for classification, pattern recognition, simulation and function approximation etc. (Jogun, 2016; Liu et al., 2020; Moayedi and Armaghani, 2018; Nguyen et al., 2019). Li and Gar-On Yeh (2004) had used ANN for the calibration of an LST model to simulate landscape pattern in a city of China and in order to do that the calibrated model provide satisfactory results. There are three layers in ANN model such as input layer, couple of hidden layers and an output layers whereas each layer has a number of neurons (Fig. 2). However, in the input layers each neuron receives one input variables and produce an output values for the next layers. Accordingly, input variables operate as signals which are passing through the layers and generate output values.

CA is one type of discrete model on modeling spatiotemporal processes (Clarke et al., 2007; Clarke and Gaydos, 1998). A CA model has five components such as space, state, time step, neighbourhood and transitional rule (Wang, 2007). Out of these five components, the space is delimitated as a trellis constituted with uniform cells which interest with each other following predefined transitional rules. At every step, the cells update their states through interacting each other. For the possibility to have number of layers in a CA model, the interaction can be done for multiple variables of each cell. Based on these repeated interaction between the cells, the model of spatial dynamics at different scale can be prepared using CA. For being a spatial model, CA model is conformable with raster data and easy to conduct in GIS. Therefore in this chapter, for the convenience of the LST simulation in CA, spatial LST data and relevant variables were transformed into shapefile with proper extension. Finally on the basis of transitional rules computed by ANN, CA can simulate future LST pattern in a raster space.

The inbuilt system of QGIS MOLUSCE is able to gather training and testing datasets. These training datasets are used to generate suitability model implementing the ANN model. Number of parameters need to be optimized to have good results in training model

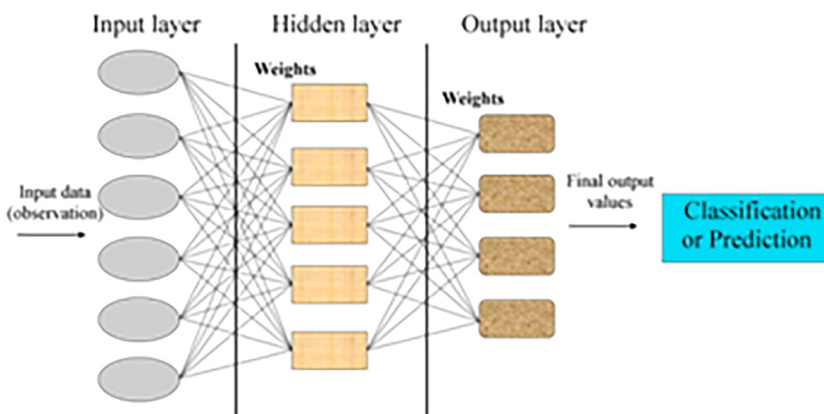


Fig. 2. Structure of a simple neural network with multiple output neurons.

using ANN. In this present work, the parameters have been fixed by trial and error process i.e. Iteration rate:1000, Learning rate:0.001, Momentum:0.02, Neighbourhood:10px, Hidden layer:10 for the optimization of the ANN model parameters. 10 pixels of neighbourhood were applied in prediction using CA. Here, at first the model was set to 1 iteration (10 years), which indicate the prediction of incoming 10 years. For the prediction of surface temperature of 2027 and 2037, transition map were prepared for previous decades. In next, applying suitability conditioning parameters of 2017, suitability model was prepared using ANN. By using suitability map, transition map, 1 iteration and 10-pixel neighbourhood, the prediction was conducted using CA model for 2027. Accordingly, the temperature of 2037 was predicted.

2.3.1. Selection of controlling variable for future LST prediction

For the simulation of future LST pattern, some landscape indices such as NDVI, NDWI, NDBI and Normalized Difference Bareness Index (NDBai) have been selected based on their strong correlation with land surface temperature (Table 2). These landscape indices are dynamic in nature over the time and associated with temperature change (Mahato and Pal, 2018; Pal and Ziaul, 2017). Therefore, for future simulation of LST, all the selected indices have been prepared for 2007, 2017 (Fig. 3), 2027 and 2037. Parameters for 2027 and 2037 have been predicted using CA and ANN because without simulating those in reference of LST predicting years, accuracy of simulation result may not be satisfactory. Beside, for the sake of validation of predicted parameters of 2027 and 2037, the same parameters or indices also simulated for 2007 and 2017 (Fig. 4) on which satellite imageries are available. Furthermore, correlation analysis has been conducted between simulated and image based controlling parameters assuming that if there is found significant correlation between them; it will be significant also in case of 2027 and 2037. For the extraction of NDVI, the Eq. (1) has been used (Townshend and Justice, 1986).

$$NDVI = \frac{(IR\ band - R\ band)}{(IR\ band + R\ band)} \quad (1)$$

where, IR is near infrared band (band 4 of MSS and TM), R is red band (MSS band 2, TM band 3). NDVI value ranges from -1 to +1 where value between 0 and 1 indicates vegetation area.

NIDWI has been extracted using the Eq. 2 (McFeeters, 1996).

$$NDWI = \frac{(Green\ band - NIR\ band)}{(Green\ band + NIR\ band)} \quad (2)$$

where, Green = the green band (MSS band 1, TM band 2) and NIR = the near-infrared band.

(band 4 of MSS and TM).

NDBI has been computed following Zha et al. (2003) (Eq. 3).

$$NDBI = \frac{(MIR - NIR)}{(MIR + NIR)} \quad (3)$$

where, MIR = the middle infrared band (TM band 5, OLI band 6) and NIR is the near infrared band (TM band 4, OLI band 5).

NDBai has been extracted using the equation of Zhao and Chen (2005) (Eq. 4).

$$NDBai = \frac{(SWIR - TIR)}{(SWIR + TIR)} \quad (4)$$

where, SWIR is Short-wave Infrared (OLI band 7, 8 and TM band 7) and TIR (OLI band 10, 11 and TM band 6).

2.4. Validation of ANN based predicted models

Cellular Automata Markov model based ANN models of 2027 and 2037 is not directly validated due to lack of data. For this ANN models of 2007 and 2017 models are prepared and the model results are compared with LST of respective periods. For comparing the simulated LST and image based LST, 241 sample sites are selected from simulated models and temperature of those sites are extracted. Based on this information, Kappa coefficient and Area under curve (AUC) in Receiver operating characteristics (ROC) are computed for

Table 2

Correlation coefficient between LST and landscape indices.

Year	Parameters	January	April	November
2007	NDVI	0.45	0.51	0.57
	NDWI	0.46	0.44	0.56
	NDBI	0.65	0.70	0.75
	NDBai	0.52	0.58	0.59
	NDVI	0.04	0.65	0.59
	NDWI	0.50	0.63	0.59
	NDBI	0.48	0.41	0.52
	NDBai	0.45	0.56	0.47

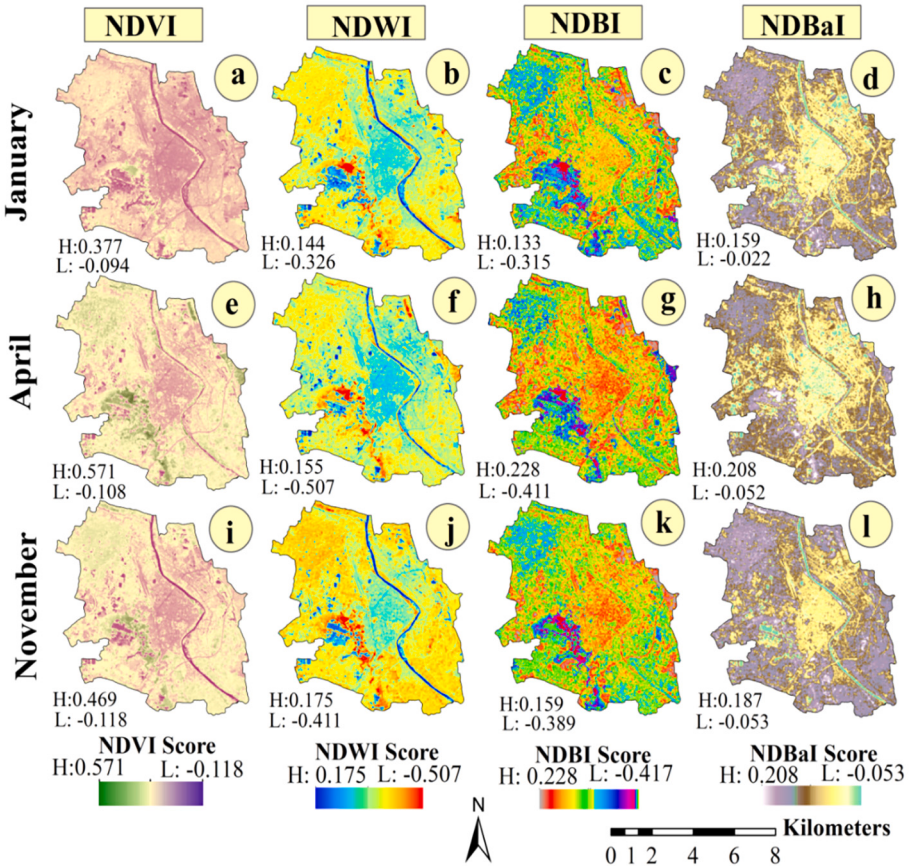


Fig. 3. Image based spatial parameters e.g. NDVI, NDWI, NDBI and NDBaI of three different months of 2017 such as (a–d) January, (e–h) April and (i–l) November.

different seasons of 2007 and 2017. It is assumed that if these models are valid it can be supposed that predicted models of 2027 and 2037 will be effective.

The ROC curve is the plot of the true positive rate against the false positive rate of different likely cut points of a diagnostic test which is frequently used to determine the accuracy of the predictive distribution model (Hiestermann and Rivers-Moore, 2015). The ROC curve deals with goodness of fit from the area it provides area under the curve. The area under ROC curve can be classified into five categories such as excellent (0.90–1.00), good (0.80–0.90), fair (0.70–0.80), poor (0.60–0.70) and fail (0.50–0.60) to demarcate the precision level (Hajian-Tilaki, 2013).

ANN based LST models of 2007 and 2017 are also correlated with image based LST of those years. High correlation between them with acceptable level of significance may help to infer the good performances of the models.

2.5. Methods for analyzing spatial pattern of temperature

For the pattern recognition of LST of the selected phases, three different approaches have been selected. In first approach, statistically significant spatial clusters of high values (hot spots) and low values (cold spots) have been identified using Getis-Ord's hot and cold spot analysis of Getis (1992). All the pixels of the LST maps of the concerned seasons are transformed into point data and based on the point specific LST values, this analysis is carried out and considering the output again point to raster conversion is done. For showing the statistical significance of the map, z-score and P-value are computed and compared with pixel level data to know the fact which pixels fall under statistically significant hot and cold spot. The following equations (Eqs. 1, 2 and 3) explain the mathematical functionalities of this analysis.

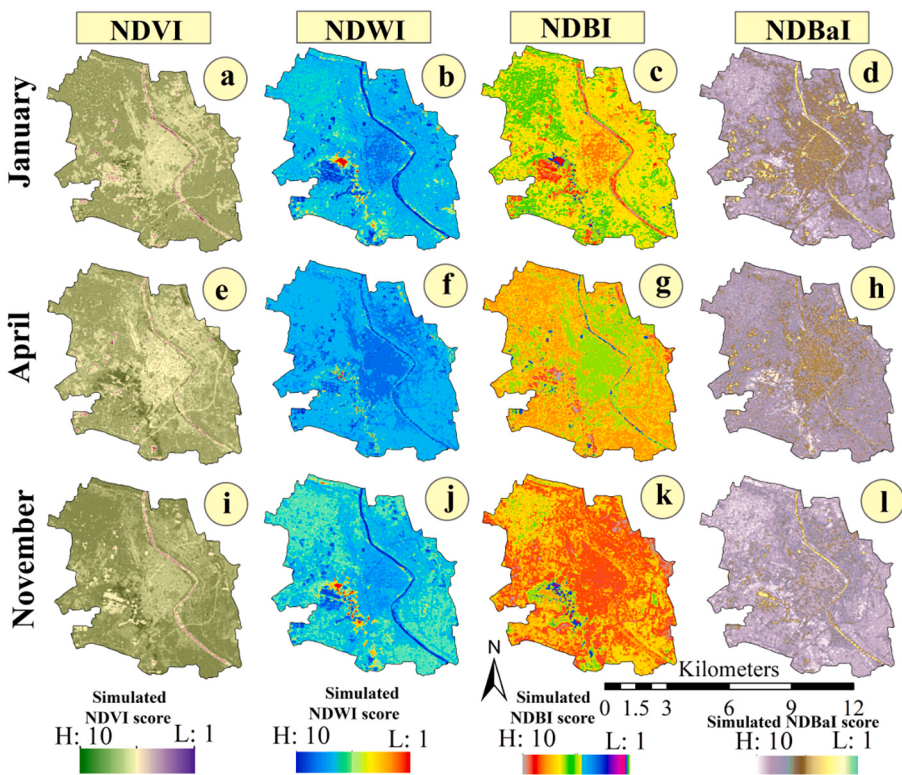


Fig. 4. Simulated spatial parameters e.g. NDVI, NDWI, NDBI and NDBaI of three different months of 2027 such as (a-d) January, (e-h) April and (i-l) November.

Table 3
Details specification of different landscape indices.

Indices	Symbols	Unit	Value	Description	References	
Area-Edge matrix	Largest Patch Index	LPI	Percent	$0 < \text{LPI} \leq 100$	LPI enumerates the percentage of total landscape area encompassed by the largest patch. As such, it simply measure dominance.	With and King (1999)
Aggregation matrix	Landscape Shape Index	LSI	None	$\text{LSI} \geq 1$, without limit	LSI quantifies a standardize evaluation of sum edge or edge density that adjusts for the size of the landscape. It is measured against a circle standard.	Herzog et al. (2001)
	Number of patch Aggregation index	NP	None	$\text{NP} \geq 1$, without limit	Number of patches in a specific patch types.	Turner et al. (1989)
	Patch Density	AI	Percent	$0 \leq \text{AI} \leq 100$	The proportion of the observed number of like adjacencies to the maximum possible number of like adjacencies in a specific patch types.	Bregt and Wopereis (1990)
		PD	Number per 100 ha	$\text{PD} > 0$, inhibited by cell size.	Number of patches in a specific patch types divided by unit area.	McGarigal and Marks (1995)

$$G_i^* = \frac{\sum_{j=1}^n w_{ij} x_j - \bar{X} \sum_{j=1}^n w_{ij}}{s \sqrt{\left[\frac{n \sum_{j=1}^n w_{ij}^2 - \left(\sum_{j=1}^n w_{ij} \right)^2}{n-2} \right]}} \quad (1)$$

where x_j is the attribute value for feature j , w_{ij} is the spatial weight between feature i and j , n is equal to the number of features and:

$$\bar{X} = \frac{\sum_{j=1}^n x_j}{n} \quad (2)$$

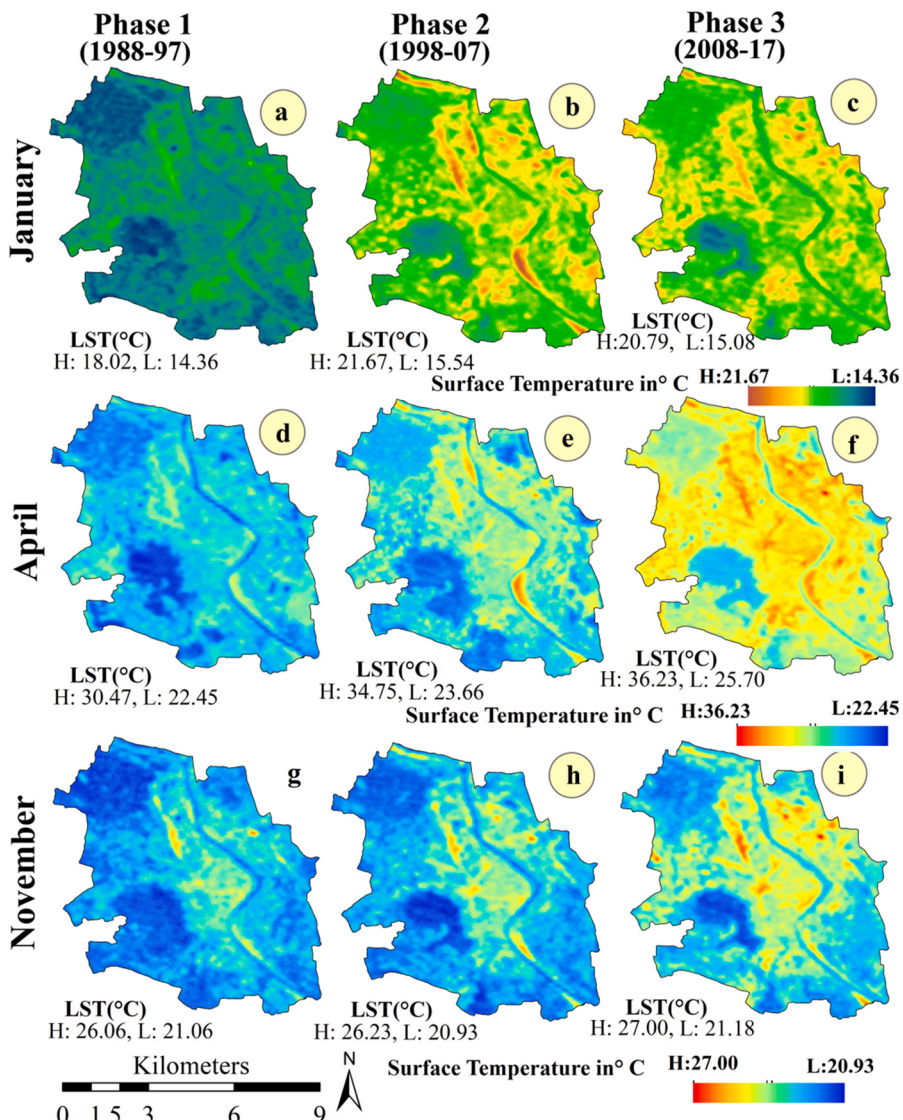


Fig. 5. Status of decadal average temperature of three different seasons in three phases such as (a) Phase 1, (b) Phase 2, and (c) Phase 3 for January; (d) Phase 1, (e) Phase 2 and (f) Phase 3 for April; (g) Phase 1, (h) Phase 2 and (i) Phase 3 for November month.

$$s = \sqrt{\frac{\sum_{j=1}^n X_j^2}{n} - (\bar{X})^2} \quad (3)$$

The G_l^* statistics is a z score so no further calculations are required.

In second approach of pattern recognition, Spatial autocorrelation measures in which extent the one pixel value (say LST) is similar or dissimilar with its surroundings pixels. Morain's I is frequently used for computing spatial autocorrelation. Morain's I value may be either positive or negative and ranges from +1 to -1. Positive spatial autocorrelation near to +1 indicates clustering of similar LST and negative value near to -1 signifies association of dissimilar LST. A value of 0 for Moran's I typically indicates no autocorrelation. Computed Z and P values help to assess whether the result is statistically significant, whether null hypothesis is to be rejected or accepted. For the determination of fragmentation of uncomfortable high and low temperature, a GIS tool (CLEAR, 2002) has been used in this present study. This tool provides the spatial information on patch, edge, core and perforated segments of uncomfortable high and low temperature. Besides for the quantification of spatial pattern of LST, FRAGSTAT (Vogt et al., 2007) is used computing several landscape indices such as number of patch (NP), patch density (PD), largest patch index (LPI), landscape shape index (LSI), aggregation index (AI). The details of those landscape indices depicted in Table 3.

3. Results

3.1. Decadal average temperature state

Decadal average temperature has been depicted in Fig. 5(a–i) of three different months such as January, April and November. In case of January, decadal average temperature ranges from 14.36 to 21.67 °C where as in case of April and November months it ranges from 22.45 to 36.23 °C and 20.93 to 27 °C respectively (Fig. 5). In January, mean temperature of phase-1 was 15.95 °C which was further increased to 17.98 °C in phase-2 and 18.00 °C in phase-3. Therefore it can be stated that over the last two decades, average temperature of January month as well as Winter season has increased about 2.05 °C. Accordingly, average temperature of April and November month also increased about 4.08 and 0.88 °C in phase-3 in reference to phase-1. For example, in April month, the mean temperature was 26.49 °C in phase-1 which was raised to 26.71 and 30.57 °C in phase-2 and phase-3 respectively (Table 4).

3.2. State of areal extension under different temperature zones

Fig. 6(a–i) shows the status of area under different temperature intensity zones in three different months e.g., January, April and November of phase-1, phase-2 and phase-3. Average LST has been calculated using multiple scenes of LST of each decade and seasons. In order to calculate area of different temperature intensity zones, the decadal average map of LST has been classified into five temperature zones with equal range of temperature (Fig. 6). In case of January month, area under <15.822 °C temperature intensity zone was 38.71% in phase-1 but over the time it decreased to 0.32% in phase-2 and in phase-3 it became 1.39%. The scenario of relatively high temperature intensity zone is quite different. For example area under the temperature intensity zones of 17.30–18.75 °C was 0.76% in January phase-1 which increased to 66.55% and 72.28% in phase-2 and phase-3 respectively (Table 5). Accordingly, area under high and very high temperature intensity zones of both April and November was observed to be increased over the phases. In April, no area found under the very high temperature intensity zone in phase-1 but in phase-2, 0.22% area appears under this temperature zone which is further increased to 2.04% in phase-3 (Table 5).

3.3. Phase wise change of decadal average temperature

Fig. 7(a–i) depicts the changes of decadal average temperature in three different phases such as phase-1, phase-2 and phase-3 of

Table 4
Descriptive statistics of decadal average temperature of three different months.

Months	Statistics	LST in degree Celsius		
		Phase 1 (1988–97)	Phase 2 (1998–2007)	Phase 3 (2008–2017)
January	Minimum	14.36	15.54	15.08
	Maximum	18.02	21.67	20.79
	Mean	15.95	17.98	18.00
	Standard deviation	0.53	0.84	0.75
April	Minimum	22.45	23.66	25.70
	Maximum	30.47	34.75	36.19
	Mean	26.49	26.71	30.57
	Standard deviation	1.29	1.69	1.68
November	Minimum	21.06	20.93	21.18
	Maximum	26.06	26.23	26.99
	Mean	22.49	22.72	23.37
	Standard deviation	0.68	0.76	0.89

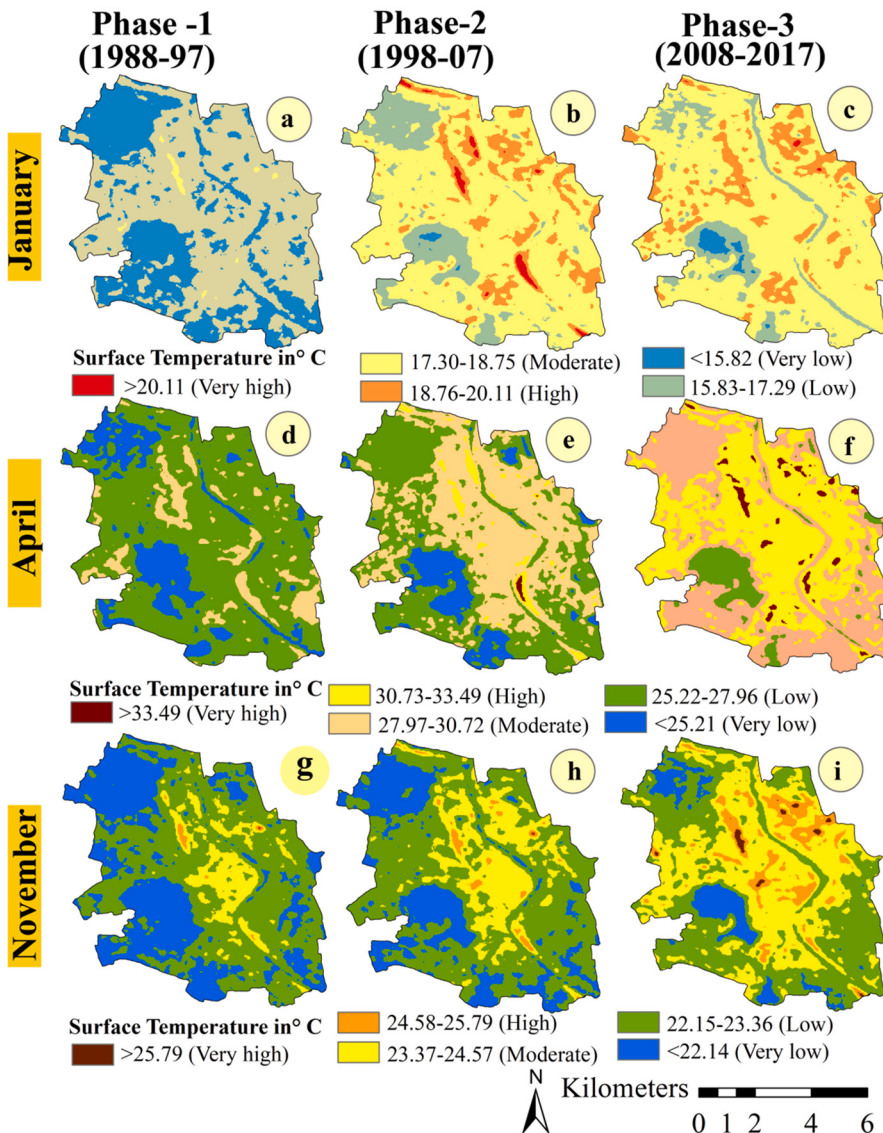


Fig. 6. Status of areal extension under different temperature zone in three different phase of three different months such as (a) Phase 1, (b) Phase 2 and (c) Phase 3 of January; (d) Phase 1, (e) Phase 2 and (f) Phase 3 of April month; (g) Phase 1, (h) Phase 2 and (i) Phase 3 of November month.

January, April and November month. In January, decadal change of average temperature ranged from -3.84 to 4.94 $^{\circ}\text{C}$ over three phases. The upper limit of phase-1, phase-2 and phase-3 in January month exhibits about 4.86 , 3.90 $^{\circ}\text{C}$ and 4.94 $^{\circ}\text{C}$ change of decadal average temperature. In case of April month, this change of LST varies from -4.65 $^{\circ}\text{C}$ to 5.47 $^{\circ}\text{C}$, -2.36 to 7.06 $^{\circ}\text{C}$ and -1.27 to 8.46 $^{\circ}\text{C}$ in phase-1, phase-2 and phase-3 respectively. In phase-3 of November month, decadal average LST change ranged from -1.34 to 4.58 $^{\circ}\text{C}$ which was -1.26 to 2.50 $^{\circ}\text{C}$ in phase-1 (Fig. 7). The upper limit of phase-3 in April months shows the maximum change of decadal average LST. Besides this, almost in case of all the phases of January, April and November month, negative change have been noticed in lower limit of decadal average LST. Therefore, it can be stated that LST has changed over time in positive and negative direction where, negative change considered as conditional phenomena.

3.4. Simulated and predicted temperature model using ANN

From the ANN based area simulated models of controlling parameters it is found that vegetated and water body area is likely to be reduced while built up area is likely to be expanded at an concerning rate in 2037. In consequence of these, LST is also predicted to be increased in all the seasons. Predicted LST models clearly demonstrate that more area is predicted to be included under high temperature range. For example, in January, area under temperature >18.66 $^{\circ}\text{C}$ is predicted to be increased from 710.54 to 2093.89 ha in between 2017 and 2037. In April 2017, 1709.73 ha area was under temperature >32.34 $^{\circ}\text{C}$ which is predicted to be increased by

Table 5

Status of areal extension under different temperature zones of January, April and November month in three different phases.

Months	Temperature zones (degree celsius)	Area (in %) under different temperature intensity zones		
		Phase-1 (1988–97)	Phase-2 (1998–2007)	Phase-3 (2008–2017)
January	<15.822	38.71	0.32	1.39
	15.83–17.29	60.53	18.11	11.80
	17.30–18.75	0.76	66.55	72.28
	18.76–20.11	–	13.78	14.16
	>20.11	–	1.23	0.11
April	<25.21	17.31	9.67	–
	25.22–27.96	71.94	43.16	7.45
	27.97–30.72	10.74	44.42	41.09
	30.73–33.49	–	2.54	49.43
	>33.49	–	0.22	2.04
November	<22.14	34.60	22.22	8.08
	22.15–23.36	54.65	56.15	41.77
	23.37–24.57	10.34	20.30	41.73
	24.58–25.79	0.40	1.32	7.82
	>25.79	0.01	0.02	0.60

4079.97 ha in 2037. Similarly, in November 2017, 2467.22 ha area was experienced with temperature $> 23.98^{\circ}\text{C}$ and area is likely to be enhanced by 3147.87 ha in 2037 (Table 6). In all the seasons, high temperature is identified in urban core area and it is likely to be expanded toward the outskirt zone. The rate of expansion is not uniform in all direction. Expansion is restricted by Chatra wetland in the west and Mango orchard in northern part of the study area (Fig. 8).

3.5. Validation of simulated LST models of 2027 and 2037

Kappa coefficient and AUC under ROC clearly show that the simulated models have fair to good agreement between image based LST and simulated LST (Fig. 9). For example, in 2007 and 2017, AUC values in January are respectively 0.75 and 0.85, in April these are 0.85 and 0.86 and in November these are 0.84 and 0.87 (Table 7). In all the cases Kappa coefficient is > 0.85 which indicates good agreement between model and image based LST in different seasons. As the simulated models of 2007 and 2017 are found as valid, it can be expected that models of 2027 and 2037 will be valid.

3.6. Analyzing spatial pattern of temperature

3.6.1. Hot spot and cold spot analysis

Fig. 10 shows hot and cold spot areas of different months in 2007 and 2017 and two predicted years 2027 and 2037. Hot and cold spot signify the concentration of high and low temperature pixels in the study area. Out of total area, 961.07 ha area experienced statistically significant cold spot in January 2017 and it is declined to 302.61 ha in 2037. On the other hand, in April 2017 significant hot spot area was 1058.85 ha which is predicted to be declined to 819.62 ha in April 2037 (Table 8). Some hot spot patches are also identified in the urban core areas which are not statistically significant. Large core area of winter season is recognized as significant cold spot but large core area of summer season is not recognized as significant hot spot rather parts of the large core is only statistically significant hot spot.

3.6.2. Spatial adjacency of LST

Spatial autocorrelation is computed for different seasons of 2007 and 2017 from observed LST and 2027 and 2037 from predicted LST. High values of Morain's I (0.74–0.99) with high Z score (255–345) and very low P value (0) (Table 9) indicates clustering of high temperature which is statistically significant. Spatial adjacency is very high in Summer season than other seasons. Over the predicted period of time there is no likelihood of significant change of such temperature distribution pattern if controlling factors remain constant. But as the urban expansion is an observed incident, more area may include under positive Morain I value carrying high temperature.

3.6.3. Fragmentation analysis

Spatial pattern of uncomfortable temperature space of two extreme ends (both cold and hot temperature) is analyzed separately and the recognized temperature space (17°C for colder end and $>33^{\circ}\text{C}$ for warmer end). In fragstat software each LST map of 2007 and 2017 of January and April months is categorized into six zones i.e. patch, edge, perforated, small core, medium and large core. Pattern of predicted virtual LST space of two extreme temperature end is also analyzed for 2027 and 2037. In the month of January, the large core cold LST is gradually transformed into medium and small core or turned into patches and over the predicted periods this transformation further be intensified. Increasing heterogeneity in land use/land covers in the peripheral land influences this transformation. On the other hand, small, medium and large core high LST of April 2007 is expanded in 2017 and predicted to enlarged in 2027 and 2037 (Fig. 11). For example, large core area was 265.41 ha in April 2007, 617.4 ha in 2017 and likely to be 3687.21 ha in 2037 (Table 10). Expansion of built up area transforming other land uses/land covers effacing heterogeneity of land is the principal

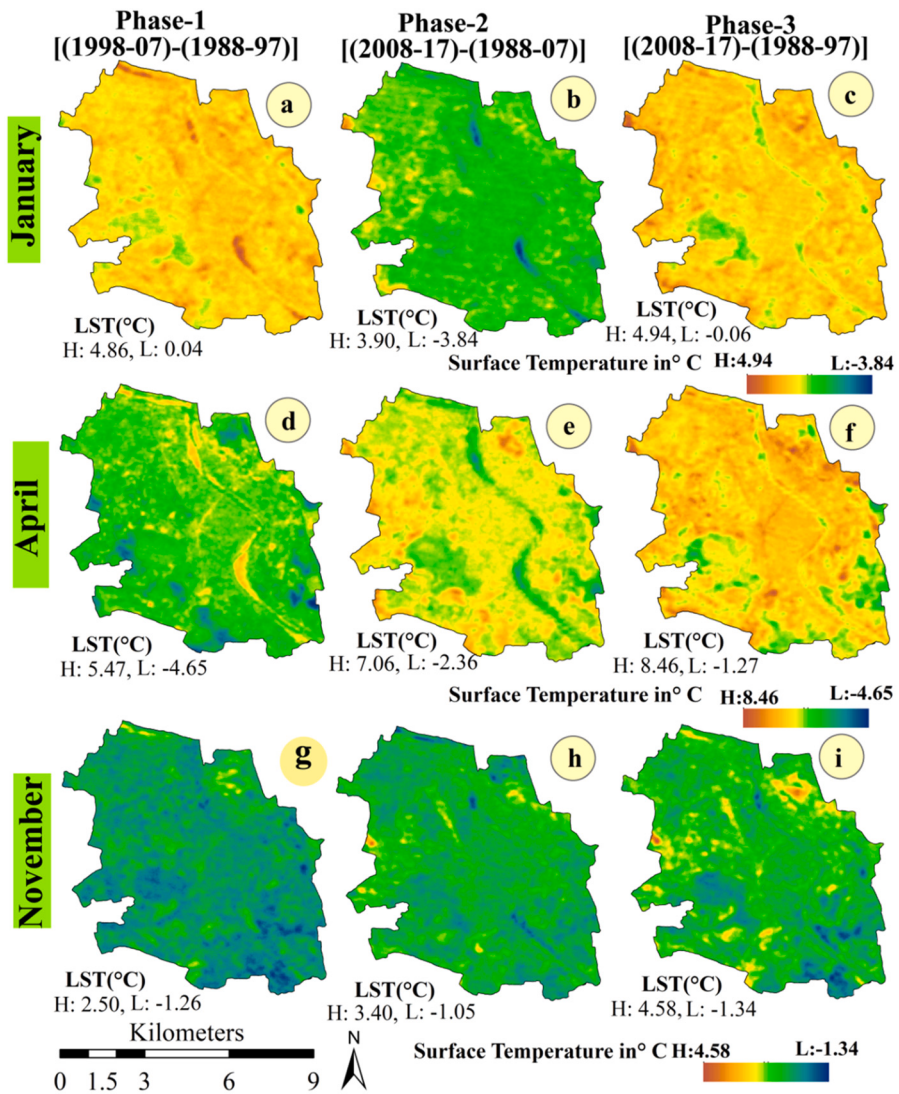


Fig. 7. Status of decadal average temperature change in three different phases of January, April and November such as Phase-1 (Change of LST between 2nd decade and 1st decade), Phase-2 (LST change between 3rd decade and 2nd decade) and Phase-3 (LST change between 3rd decade and 1st decade).

reason behind such growing large core LST area.

Table 11 also clearly demonstrates the changing fragmentation pattern of high and low LST. Patch frequency, density, are increased over time in case of low temperature and declined in case of high temperature. Largest Patch Index (LPI) is declined in Winter time (January) (9.19 to 0.67) and increased in Summer season (April) (7.66 to 75.44). Decreasing Aggregation index (AI) (91.46 to 32.61) and Mean contiguity (0.59 to 0.08) in Winter and increasing the same in Summer seasons from 2007 to 2037 also established the land use transformation theory.

4. Discussion

Land surface temperature is considered as an important parameter to recognize the UHI phenomena. Recognition of spatial distribution pattern, temporal trend and its impact can play important role in removal of urban heat island effects. Therefore this present study emphasizes on calculation of season wise spatio-temporal LST and its trend detection. For the extraction of LST of all the selected years and selected seasons, radiative transfer equation method has been used. In order to analyze the changing trend of LST, least square regression is used for both spatial and numerical LST datasets. From the result of long term spatial distribution of LST, it is noticed that in all three seasons such as Winter, Summer and Post Monsoon, the surface temperature of both the upper end and lower end is gradually rising over the time. For example, in Summer season of 1990, the upper end LST was recorded as 32.45 °C which increased to 35.79 °C in 2016 where as the lower end LST grown from 21.34 °C in 1990 to 23.92 °C in 2016. Similarly the temperature

Table 6
Area under different temperature intensity zones.

Months	Temperature zones (degree celsius)	Area (in ha) under different temperature intensity zones			
		2007	2017	2027	2037
January	<15.63	86.05	196.45	78.66	36.99
	15.64–17.14	2136.49	1235.70	614.58	282.97
	17.15–18.65	2811.83	3300.06	4041.09	3029.52
	18.66–20.16	401.15	710.54	728.17	2093.89
	>20.16	29.91	22.69	2.93	22.07
April	<26.72	188.91	198.24	218.91	218.07
	26.73–29.53	815.34	595.45	261.51	261.02
	29.54–32.34	3166.81	2953.28	1808.49	767.93
	32.35–35.15	1280.86	1709.73	3037.14	4079.97
	>35.15	13.51	8.73	139.37	138.45
November	<22.51	2107.57	280.98	67.17	62.27
	22.52–23.98	2652.94	2272.94	2499.44	1618.67
	23.99–25.44	698.17	2467.22	2181.12	3147.87
	25.44–26.9	6.75	426.28	709.89	628.94
	>26.9		18.01	7.81	7.68

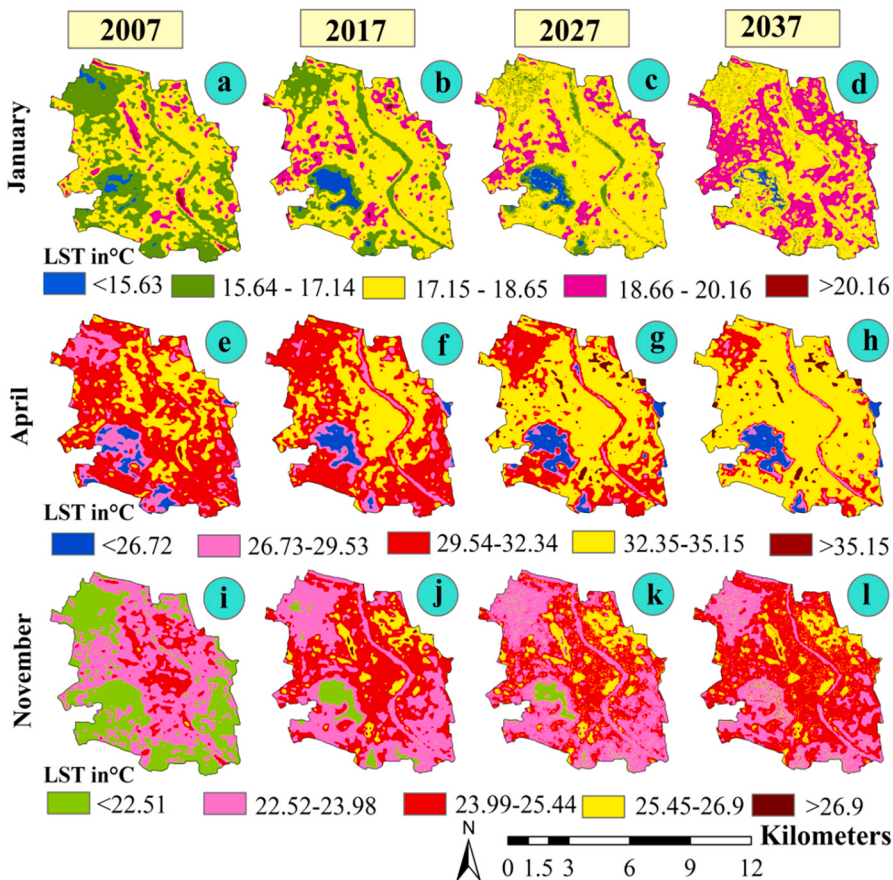


Fig. 8. Simulated LST models for different months such as January, April and September of 2007, 2017, 2027 and 2037.

of Winter and Post Monsoon is increased. Pal and Ziaul (2017) in their previous study have reported that the built up area of this present study area has increased tremendously while the natural surfaces specifically water body and vegetation have shranked over the time. According to Luyssaert et al. (2014) and Zhao et al. (2018), there are approaching connection of LST with LULC types, land use layout and landscape fabric. Therefore fleeting urbanization can alter the fundamental surface (Julien et al., 2011; Zhou et al., 2011) which reinforce the UHI consequences. With rising LST in all three season, the area under high temperature intensity zones also enlarged. For example, in April or Summer season, no area noticed under the very temperature intensity zone ($>33.49^{\circ}\text{C}$) in phase-1

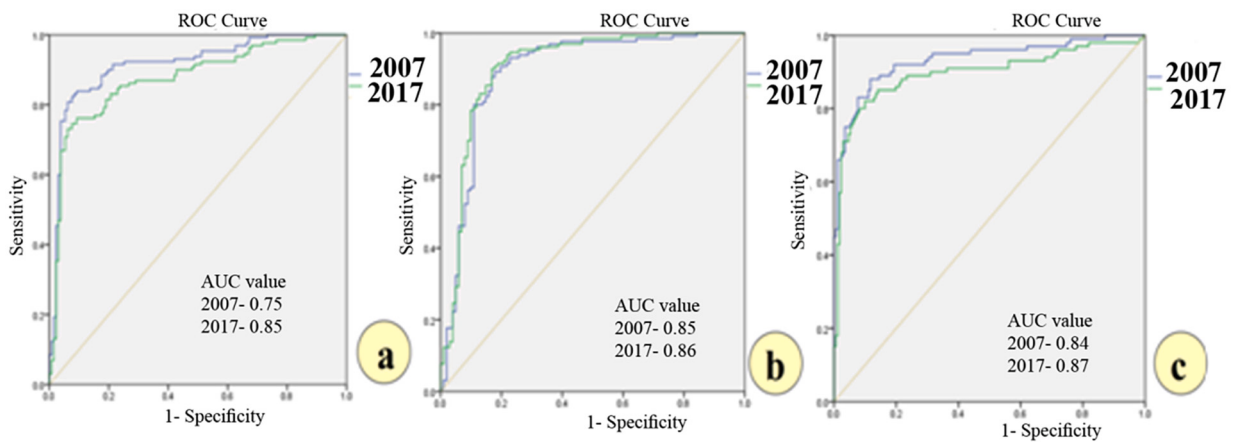


Fig. 9. ROC of LST for three different months of 2007 and 2017 such as (a) January, (b) April and (c) November.

Table 7
Kappa coefficient and AUC under ROC in different months of 2007 and 2017.

Year/month	Kappa coefficient			AUC			Correlation coefficient		
	January	April	November	January	April	November	January	April	November
2007	0.82	0.84	0.86	0.75	0.85	0.84	0.61	0.73	0.59
2017	0.85	0.87	0.84	0.85	0.86	0.87	0.69	0.81	0.77

(1988–1997) but in phase-2 (1998–2007), 12.06 ha area come out under this temperature zone which is further enlarged to 111.54 ha in phase-3 (2008–2017).

Urban growth is a very progressive phenomenon over the globe and it is established that such rapid urban growth has direct influence on urban landscape and temperature change. Therefore it is essential to understand impact of landscape transformation on future temperature. In this present study, the future temperature pattern has been predicted for three different months e.g. January, April and November using three different methods and techniques such as ANN, linear regression and SVM. In order to predict future temperature pattern based on ANN approach, various land surface parameters e.g. NDVI, NDWI, NDBI and NDBAI have been applied. The application of ANN model has given more plausible results because it considers perplexing datasets and also acting with non linear structures. In this present study the ANN results of future LST simulation reveals that in January, area under temperature $> 18.66^{\circ}\text{C}$ is anticipated to be enlarged from 710.54 ha in 2017 to 2093.89 ha in 2037. In case of April month, 1709.97 ha area was under temperature $> 32.34^{\circ}\text{C}$ in 2017 which is expected to be enlarged by 4079.97 ha in 2037. Therefore it can be stated that area under high temperature intensity zone will be increase over the time due the change in LULC. The prior studies also indicated that the rising of future temperature is significantly related with urban growth allied LULC changes ([Amiri et al., 2009](#); [Li et al., 2009](#); [McCarthy et al., 2010](#); [Nayak and Mandal, 2012](#); [Odindi et al., 2015](#)).

In this study, couple of methodological approaches such as hot spot and cold spot analysis, spatial autocorrelation analysis and fragmentation analysis has been considered to analyze the spatio-temporal pattern of LST and to recognize the consistence thermal hot spot and cold spot. Identification of thermal hot and cold spot can help in designing UHI removal plans of urban areas ([Ranagalage et al., 2018](#); [Mavrikou et al., 2018](#)). Therefore, considering the implication of pattern analysis of LST, spatio-temporal thermal hot spot and cold spot has been ascertained using Getis-Ord's method. From results of hot and cold spot analysis, it has been observed that all the cold spot exists over the water body and vegetated area. In this context couple of researchers already stated that vegetation can play important role in reduction of LST effects ([Adeyeri and Okogbuo, 2014](#)). It is estimated that about 961.07 ha area comes under the statistically significant cold spot in January 2017 but in 2037 it is predicted to be declined to 302.61 ha. Similar kind of result has been found in case of hot spot area, for example in 2037 area under significant hot spot predicted to be declined from 1058.85 ha in 2017 to 819.62 ha because simultaneously area of under statistically insignificant hot spot area has increased which may appear as significant hot spot in next few decades.

In the second approach of this study, it has been recognized that the spatial adjacency of LST both in actual and predicted years is very high in summer season than other season. If the controlling factors remains constant in upcoming decades than there will be no likelihood of significant change of such spatial adjacency or distributional pattern of LST. [Pal and Ziaul \(2017\)](#) reported that natural land covers over such as vegetation, water body are shrinking due to the rapid urban growth. Therefore it can be predicted that due to the rapid urban growth, more area may include under positive Morain I value. Accordingly spatial fragmentation analysis of LST shows the two types of transformation such as the large core of January month fragmented into medium core and patches over the time whereas medium and small core of uncomfortable high temperature in April month transformed into large core over the last two decades and it is predicted that this large core further will be enlarge. Similarly patch frequency, density, are increased over time in

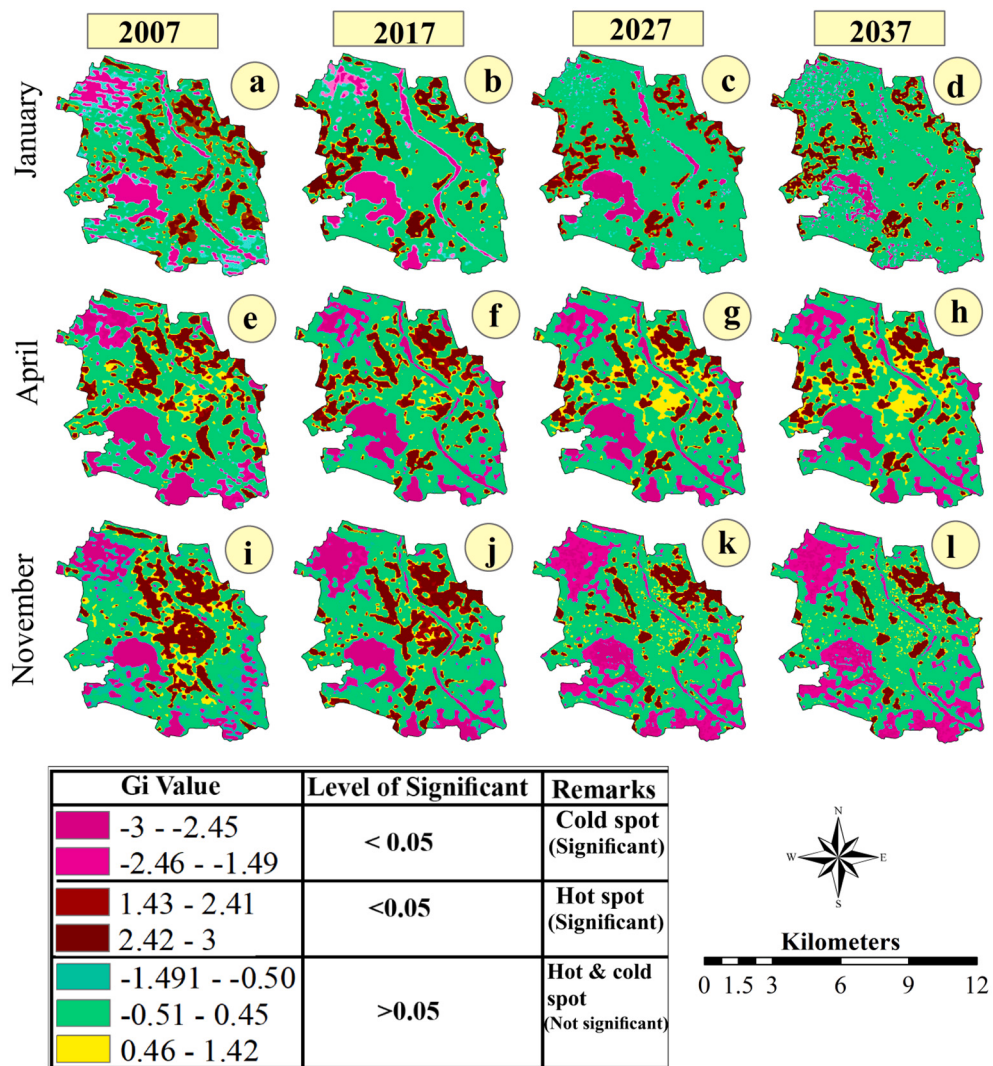


Fig. 10. Hot and cold spot area identified using Getis-ord method in 2007, 2017, 2027 and 2037.

Table 8
Area under different hot spot and cold spot zones.

Year	Month	Area (in ha.) under different thermal zones		
		Hot spot (significant)	Cold spot (significant)	Hot and cold spot (not significant)
2007	January	1046.24	787.41	3631.78
	April	1067.36	649.87	3748.20
	November	1100.96	546.34	3818.13
2017	January	961.07	420.11	4084.25
	April	1058.85	573.97	3832.61
	November	1103.11	627.32	3735.00
2027	January	794.25	293.21	4377.97
	April	837.54	662.70	3965.19
	November	619.39	1303.31	3542.73
2037	January	302.61	755.24	4407.58
	April	819.62	663.13	3982.68
	November	563.84	1396.02	3505.57

Table 9

Morain's I value, Z score and P values of the LST model computed from Landsat images.

Year	Month	Morain I	Z score	P value
2007	January	0.99	345.83	0
	April	0.98	341.35	0
	November	0.97	335.71	0
2017	January	0.98	341.90	0
	April	0.99	342.11	0
	November	0.98	342.61	0
2027	January	0.86	300.07	0
	April	0.96	333.71	0
	November	0.86	300.16	0
2037	January	0.74	255.80	0
	April	0.95	332.35	0
	November	0.85	296.49	0

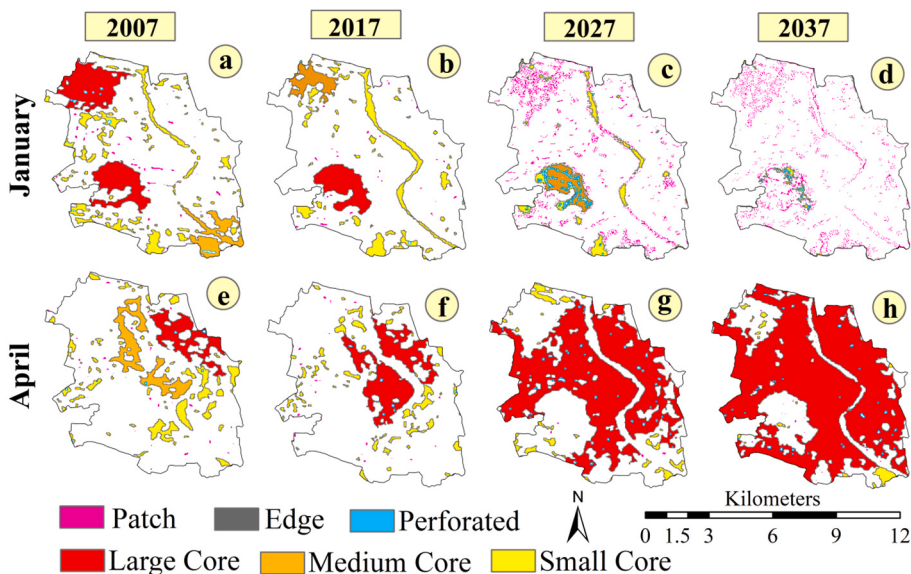


Fig. 11. Predicted uncomfortable temperature pattern in Winter (January) and Summer (April) based on Fragmentation analysis for the month of January and April in different years e.g. (a) January 2007 (b) January 2017 (c) January 2027 and (d) January 2037 (e) April 2007 (f) April 2017 (g) April 2027 and (h) April 2037.

Table 10

Area under different fragmentation zones in different phase of January and April.

Fragmentation zones	January (area in hectare)				April (area in hectare)			
	2007	2017	2027	2037	2007	2017	2027	2037
Patches	26.37	14.94	273.78	250.92	13.95	12.24	4.59	4.41
Small core	317.79	300.33	120.24	9.9	285.93	174.6	122.58	58.32
Medium core	172.17	140.58	133.83		296.1			
Large core	645.39	279.36			265.41	617.4	2502.72	3687.21

case of low temperature and declined in case of high temperature. The main reason behind such kind of changing pattern of LST is rapid expansion of impervious surface, shrinking of vegetated and water body area, anthropogenic activity (Pal and Ziaul, 2017; Ziaul and Pal, 2018). Besides excessive metallic composition in building materials is another cause of temperature rise because it can retain additional heat (Skarbit et al., 2017). This study can support in UHI mitigation plans providing information about consistent thermal hot spot and cold spot as well as changing pattern of LST. Furthermore it suggest to preserve vegetation and water body specifically adjacent urban wetland for reducing expansion of large core area of uncomfortable high temperature as well as number of significant hot spots.

Table 11

Fragmentation indices depicting pattern of extreme temperature during winter and summer season.

Season	Year	NP	PD	LPI	AI	CONTIG_MN	LSI
January	2007	109	1.99	9.19	91.46	0.59	12.47
	2017	82	1.50	5.88	91.27	0.59	10.40
	2027	627	11.48	5.03	66.27	0.17	31.88
	2037	1240	22.69	0.67	32.61	0.08	41.75
April	2007	88	1.61	7.66	90.98	0.616	11.71
	2017	75	1.37	9.06	91.62	0.609	10.50
	2027	35	0.64	35.27	95.96	0.63	8.48
	2037	31	0.57	75.44	97.33	0.35	6.69

5. Conclusion

The present study explored that pixel wise phasal change of LST ranges from -3.84 to 4.94 °C in the month of January, -4.65 to 8.46 °C in the month of April and -1.34 to 4.58 °C in the month of September. From average temperature change in different phases, the fact of temperature rise is very prominent. ANN based predicted LST models clearly predicted the inclusion of wider area under high temperature range. For example, in April 2017, 1709.73 ha area was under temperature > 32.34 °C which is predicted to be increased by 4079.97 ha in 2037. Spatial pattern of temperature specifically high and low temperature of existing LST of 2007 and 2017 and predicted LST of 2027 and 2037 is analyzed using spatial autocorrelation, hot spot analysis and fragmentation indices. Statistically significant high and low temperature clustering is recognized both during high and low temperature. In case of low temperature large core area is gradually decreased and predicted to be decreased in 2027 and 2037. But extent of large core area is gradually increased over the period of time in case of high temperature. These are also properly reflected by fragmentation indices like NP, PD, LPI, AI and mean contiguity. Statistically significant cold spot is identified in the water logged and vegetative areas and hot spot is identified in the urban mainland. As surface parameters play significant role for controlling spatial temperature difference, rising temperature and changing spatial pattern of temperature distribution, so minimizing strategies should emphasize on those parameters. Increase of green space through plantation along road sides, vacant public space, river banks, roof top plantation are some means of minimizing temperature effect. ENVI-met software based modeling in this regard has also proved that different forms of plantation strategies may reduce temperature by 1–2 °C (Ziaul and Pal, 2020).

Declaration of Competing Interest

None.

References

- Adeyeri, O.E., Okogbue, E.C., 2014. Effect of landuse landcover on land surfacetemperature. In: Proceedings of the Climate Change, and Sustainable EconomicDevelopment, pp. 175–184.
- Agathangelidis, I., Cartalis, C., Santamouris, M., 2016. Estimation of air temperatures for the urban agglomeration of Athens with the use of satellite data. Geoinform. Geostat. 4 (2), 2–7.
- Ahmed, B., Kamruzzaman, M., Zhu, X., Rahman, M., Choi, K., 2013. Simulating land cover changes and their impacts on land surface temperature in Dhaka, Bangladesh. Remote Sens. 5 (11), 5969–5998.
- Akbari, H., Cartalis, C., Kolokotsa, D., Muscio, A., Pisello, A.L., Rossi, F., Zinzi, M., 2016. Local climate change and urban heat island mitigation techniques—the state of the art. J. Civ. Eng. Manag. 22 (1), 1–16.
- Alsarraf, J., Moayedi, H., Rashidi, A.S.A., Muazu, M.A., Shahsavar, A., 2020. Application of PSO-ANN modelling for predicting the exergetic performance of a building integrated photovoltaic/thermal system. Eng. Comput. 36 (2), 633–646.
- Amiri, R., Weng, Q., Alimohammadi, A., Alavipanah, S.K., 2009. Spatial–temporal dynamics of land surface temperature in relation to fractional vegetation cover and land use/cover in the Tabriz urban area, Iran. Remote Sens. Environ. 113 (12), 2606–2617.
- Artis, D.A., Carnahan, W.H., 1982. Survey of emissivity variability in thermography of urban areas. Remote Sens. Environ. 12 (4), 313–329.
- Bregt, A.K., Wopereis, M.C.S., 1990. Comparison of complexity measures for choropleth maps. Cartogr. J. 27 (2), 85–91.
- Chakraborty, T., Sarangi, C., Tripathi, S.N., 2017. Understanding diurnality and inter-seasonality of a sub-tropical urban heat island. Bound.-Layer Meteorol. 163 (2), 287–309.
- Chen, E., Allen Jr., L.H., Bartholic, J.F., Gerber, J.F., 1983. Comparison of winter-nocturnal geostationary satellite infrared-surface temperature with shelter—height temperature in Florida. Remote Sens. Environ. 13 (4), 313–327.
- Chen, X.L., Zhao, H.M., Li, P.X., Yin, Z.Y., 2006. Remote sensing image-based analysis of the relationship between urban heat island and land use/cover changes. Remote Sens. Environ. 104 (2), 133–146.
- Choubin, B., Abdolshahnejad, M., Moradi, E., Querol, X., Mosavi, A., Shamshirband, S., Ghamisi, P., 2020. Spatial hazard assessment of the PM10 using machine learning models in Barcelona, Spain. Sci. Total Environ. 701, 134474.
- Chudnovsky, A., Ben-Dor, E., Saaroni, H., 2004. Diurnal thermal behavior of selected urban objects using remote sensing measurements. Energy Build. 36 (11), 1063–1074.
- Clarke, K.C., Gaydos, L.J., 1998. Loose-coupling a cellular automaton model and GIS: long-term urban growth prediction for San Francisco and Washington/Baltimore. Int. J. Geogr. Inf. Sci. 12 (7), 699–714.
- Clarke, K.C., Gazulis, N., Dietzel, C., Goldstein, N.C., 2007. A decade of SLEUTHing: Lessons learned from applications of a cellular automaton land use change model. In: Classics in IJGIS: twenty years of the international journal of geographical information science and systems, pp. 413–427.
- CLEAR, 2002. Forest Fragmentation in Connecticut: 1985–2006. Center for Land Use Education and Research. <http://clear.uconn.edu/projects/landscape/forestfrag> (Accessed 05 May 2015).
- Coutts, A.M., Harris, R.J., Phan, T., Livesley, S.J., Williams, N.S., Tapper, N.J., 2016. Thermal infrared remote sensing of urban heat: hotspots, vegetation, and an assessment of techniques for use in urban planning. Remote Sens. Environ. 186, 637–651.

- Deng, C., Wu, C., 2013. Examining the impacts of urban biophysical compositions on surface urban heat island: a spectral unmixing and thermal mixing approach. *Remote Sens. Environ.* 131, 262–274.
- Friedl, M.A., 2002. Forward and inverse modeling of land surface energy balance using surface temperature measurements. *Remote Sens. Environ.* 79 (2–3), 344–354.
- Gallo, K., Hale, R., Tarpley, D., Yu, Y., 2011. Evaluation of the relationship between air and land surface temperature under clear-and cloudy-sky conditions. *J. Appl. Meteorol. Climatol.* 50 (3), 767–775.
- Goggins, W.B., Chan, E.Y., Ng, E., Ren, C., Chen, L., 2012. Effect modification of the association between short-term meteorological factors and mortality by urban heat islands in Hong Kong. *PLoS One* 7 (6), e38551.
- Hajian-Tilaki, K., 2013. Receiver operating characteristic (ROC) curve analysis for medical diagnostic test evaluation. *Caspian J. Intern. Med.* 4 (2), 627.
- Handayani, H.H., Estoqe, R.C., Murayama, Y., 2018. Estimation of built-up and green volume using geospatial techniques: a case study of Surabaya, Indonesia. *Sustain. Cities Soc.* 37, 581–593.
- Hasanlou, M., Mostofi, N., 2015. Investigating urban heat island estimation and relation between various land cover indices in Tehran city using Landsat 8 imagery. In: Proceedings of the 1st International Electronic Conference on Remote Sensing, Basel, Switzerland, pp. 1–11.
- Herzog, F., Lausch, A., Müller, E., Thulke, H.H., Steinhardt, U.T.A., Lehmann, S., 2001. Landscape metrics for assessment of landscape destruction and rehabilitation. *Environ. Manag.* 27 (1), 91–107.
- Hiestermann, J., Rivers-Moore, N., 2015. Predictive modelling of wetland occurrence in KwaZulu-Natal, South Africa. *S. Afr. J. Sci.* 111 (7–8), 1–10.
- Jain, A.K., Mao, J., Mohiuddin, K.M., 1996. Artificial neural networks: a tutorial. *Computer* 3, 31–44.
- Jogun, T., 2016. The simulation model of land cover change in the Požega-Slavonia County (Doctoral Dissertation, Prirodoslovno-matematički Fakultet, Geografski Odjek, Sveučilište U Zagrebu).
- Julien, Y., Sobrino, J.A., Jiménez-Muñoz, J.C., 2011. Land use classification from multitemporal Landsat imagery using the yearly land cover dynamics (YLCD) method. *Int. J. Appl. Earth Obs. Geoinf.* 13 (5), 711–720.
- Kuang, W.H., Zhang, S.W., Liu, J.Y., SHAO, Q., 2010. Methodology for classifying and detecting intra-urban land use change: a case study of Changchun city during the last 100 years. *J. Remote Sens.* 14 (2), 345–355.
- Landsat Project Science Office. Landsat 7 Science Data User's Handbook. URL: http://lpwww.gsfc.nasa.gov/IAS/handbook/handbook_toc.html (last date accessed: 10 September 2003).
- Le, L.T., Nguyen, H., Zhou, J., Dou, J., Moayed, H., 2019. Estimating the heating load of buildings for smart city planning using a novel artificial intelligence technique PSO-XGBoost. *Appl. Sci.* 9 (13), 2714.
- Li, H., Liu, Q., 2008, December. Comparison of NDBI and NDVI as indicators of surface urban heat island effect in MODIS imagery. In: International Conference on Earth Observation Data Processing and Analysis (ICEODPA), vol. 7285. International Society for Optics and Photonics (p. 728503).
- Li, J.J., Wang, X.R., Wang, X.J., Ma, W.C., Zhang, H., 2009. Remote sensing evaluation of urban heat island and its spatial pattern of the Shanghai metropolitan area, China. *Ecol. Complex.* 6 (4), 413–420.
- Li, X., Gar-On Yeh, A., 2004. Data mining of cellular automata's transition rules. *Int. J. Geogr. Inf. Sci.* 18 (8), 723–744.
- Li, X., Li, W., Middel, A., Harlan, S.L., Brazel, A.J., Turner II, B.L., 2016a. Remote sensing of the surface urban heat island and land architecture in Phoenix, Arizona: combined effects of land composition and configuration and cadastral-demographic-economic factors. *Remote Sens. Environ.* 174, 233–243.
- Li, Z., Liu, S., Zhang, X., West, T.O., Ogle, S.M., Zhou, N., 2016b. Evaluating land cover influences on model uncertainties—a case study of cropland carbon dynamics in the mid-continent intensive campaign region. *Ecol. Model.* 337, 176–187.
- Li, L., Moayed, H., Rashid, A.S.A., Rahman, S.S.A., Nguyen, H., 2020. Optimizing an ANN model with genetic algorithm (GA) predicting load-settlement behaviours of eco-friendly raft-pile foundation (ERP) system. *Eng. Comput.* 36 (1), 421–433.
- Luo, M., Lau, N.C., 2017. Heat waves in southern China: synoptic behavior, long-term change, and urbanization effects. *J. Clim.* 30 (2), 703–720.
- Luysaert, S., Jammes, M., Stoy, P.C., Estel, S., Pongratz, J., Ceschia, E., Gielen, B., 2014. Land management and land-cover change have impacts of similar magnitude on surface temperature. *Nat. Clim. Chang.* 4 (5), 389.
- Mahato, S., Pal, S., 2018. Changing land surface temperature of a rural Rarh tract river basin of India. *Remote Sens. Appl.: Soc. Environ.* 10, 209–223.
- Majumdar, D.D., Biswas, A., 2016. Quantifying land surface temperature change from LISA clusters: an alternative approach to identifying urban land use transformation. *Landsc. Urban Plan.* 153, 51–65.
- Markham, B.L., Barker, J.L., 1985. Spectral characterization of the Landsat thematic mapper sensors. *Int. J. Remote Sens.* 6 (5), 697–716.
- Mavrikou, T., Polydoros, A., Cartalis, C., Santamouris, M., 2018. Recognition of thermal hot and cold spots in urban areas in support of mitigation plans to counteract overheating: application for Athens. *Climate* 6 (1), 16.
- McCarthy, M.P., Best, M.J., Betts, R.A., 2010. Climate change in cities due to global warming and urban effects. *Geophys. Res. Lett.* 37 (9).
- McFeeters, S.K., 1996. The use of the normalized difference water index (NDWI) in the delineation of open water features. *Int. J. Remote Sens.* 17 (7), 1425–1432.
- McGarigal, K., Marks, B.J., 1995. FRAGSTATS: spatial pattern analysis program for quantifying landscape structure. In: Gen. Tech. Rep. PNW-GTR-351. Portland, OR: US Department of Agriculture, Forest Service, Pacific Northwest Research Station (122 p, 351).
- Moayed, H., Armaghani, D.J., 2018. Optimizing an ANN model with ICA for estimating bearing capacity of driven pile in cohesionless soil. *Eng. Comput.* 34 (2), 347–356.
- Mohan, M., Kandy, A., 2015. Impact of urbanization and land-use/land-cover change on diurnal temperature range: a case study of tropical urban airshed of India using remote sensing data. *Sci. Total Environ.* 506, 453–465.
- Mushore, T.D., Odindi, J., Dube, T., Mutanga, O., 2017. Prediction of future urban surface temperatures using medium resolution satellite data in Harare metropolitan city, Zimbabwe. *Build. Environ.* 122, 397–410.
- Nayak, S., Mandal, M., 2012. Impact of land-use and land-cover changes on temperature trends over Western India. *Curr. Sci.* 1166–1173.
- Nguyen, H., Bui, X., Tran, Q., Moayed, H., 2019. Predicting blast-induced peak particle velocity using BGAMs, ANN and SVM: a case study at the Nui Beo open-pit coal mine in Vietnam. *Environ. Earth Sci.* 78, 479.
- Nichol, J.E., Fung, W.Y., Lam, K.S., Wong, M.S., 2009. Urban heat island diagnosis using ASTER satellite images and 'in situ' air temperature. *Atmos. Res.* 94 (2), 276–284.
- Odindi, J.O., Bangawabo, V., Mutanga, O., 2015. Assessing the Value of UrbanGreen spaces in Mitigating Multi-Seasonal Urban heat using MODIS Land Surface Temperature (LST) and Landsat 8 data. *Int. J. Environ. Res.* 9 (1), 9–18.
- Pal, S., Ziaul, S.K., 2017. Detection of land use and land cover change and land surface temperature in English Bazar urban centre. *Egypt. J. Remote Sens. Space Sci.* 20 (1), 125–145.
- Patz, J.A., Campbell-Lendrum, D., Holloway, T., Foley, J.A., 2005. Impact of regional climate change on human health. *Nature* 438 (7066), 310.
- Ranagalage, M., Estoqe, R., Zhang, X., Murayama, Y., 2018. Spatial changes of urban heat island formation in the Colombo District, Sri Lanka: implications for sustainability planning. *Sustainability* 10 (5), 1367.
- Rauner, S., Eichhorn, M., Thrän, D., 2016. The spatial dimension of the power system: investigating hot spots of smart renewable power provision. *Appl. Energy* 184, 1038–1050.
- Rizwan, A.M., Dennis, L.Y., Chunho, L.I.U., 2008. A review on the generation, determination and mitigation of urban Heat Island. *J. Environ. Sci.* 20 (1), 120–128.
- Saitoh, T.S., Shimada, T., Hoshi, H., 1996. Modeling and simulation of the Tokyo urban heat island. *Atmos. Environ.* 30 (20), 3431–3442.
- Seto, K.C., Güneralp, B., Hutyra, L.R., 2012. Global forecasts of urban expansion to 2030 and direct impacts on biodiversity and carbon pools. *Proc. Natl. Acad. Sci.* 109 (40), 16083–16088.
- Skarbit, N., Stewart, I.D., Unger, J., Gál, T., 2017. Employing an urban meteorological network to monitor air temperature conditions in the 'local climate zones' of Szeged, Hungary. *Int. J. Climatol.* 37, 582–596.
- Snyder, W.C., Wan, Z., Zhang, Y., Feng, Y.Z., 1998. Classification-based emissivity for land surface temperature measurement from space. *Int. J. Remote Sens.* 19 (14), 2753–2774.
- Songchitruksa, P., Zeng, X., 2010. Getis–Ord spatial statistics to identify hot spots by using incident management data. *Transp. Res. Rec.* 2165 (1), 42–51.

- Stathopoulou, M., Cartalis, C., 2009. Downscaling AVHRR land surface temperatures for improved surface urban heat island intensity estimation. *Remote Sens. Environ.* 113 (12), 2592–2605.
- Sun, Y., Zhang, X., Ren, G., Zwiers, F.W., Hu, T., 2016. Contribution of urbanization to warming in China. *Nat. Clim. Chang.* 6 (7), 706.
- Townshend, J.R., Justice, C.O., 1986. Analysis of the dynamics of African vegetation using the normalized difference vegetation index. *Int. J. Remote Sens.* 7 (11), 1435–1445.
- Tsai, P.J., Lin, M.L., Chu, C.M., Perng, C.H., 2009. Spatial autocorrelation analysis of health care hotspots in Taiwan in 2006. *BMC Public Health* 9 (1), 464.
- Turner, M.G., Gardner, R.H., Dale, V.H., O'Neill, R.V., 1989. Predicting the spread of disturbance across heterogeneous landscapes. *Oikos* 52 (1), 121–129.
- Unganai, L.S., 1996. Historic and future climatic change in Zimbabwe. *Clim. Res.* 6 (2), 137–145.
- Valsson, S., Bharat, A., 2009. Urban heat island: cause for microclimate variations. *Archit.-Time Space People* 2125.
- Vogt, P., Riitters, K.H., Estreguil, C., Kozak, J., Wade, T.G., Wickham, J.D., 2007. Mapping spatial patterns with morphological image processing. *Landscape Ecol.* 22 (2), 171–177.
- Wang, F., 2007. Land-Cover and Land-Use Study Using Genetic Algorithms, Petri Nets, and Cellular Automata.
- Weng, Q., Lu, D., Schubring, J., 2004. Estimation of land surface temperature–vegetation abundance relationship for urban heat island studies. *Remote Sens. Environ.* 89 (4), 467–483.
- With, K.A., King, A.W., 1999. Extinction thresholds for species in fractal landscapes. *Conserv. Biol.* 13 (2), 314–326.
- Wolf, T., McGregor, G., 2013. The development of a heat wave vulnerability index for London, United Kingdom. *Weather Clim. Extremes* 1, 59–68.
- Xu, L.Y., Xie, X.D., Li, S., 2013. Correlation analysis of the urban heat island effect and the spatial and temporal distribution of atmospheric particulates using TM images in Beijing. *Environ. Pollut.* 178, 102–114.
- Yuan, F., Bauer, M.E., 2007. Comparison of impervious surface area and normalized difference vegetation index as indicators of surface urban heat island effects in Landsat imagery. *Remote Sens. Environ.* 106 (3), 375–386.
- Yun, S.B., Yoon, S.H., Ju, S., Oh, W.S., Ma, J.W., Heo, J., 2016, October. Taxi cab service optimization using spatio-temporal implementation to hot-spot analysis with taxi trajectories: a case study in Seoul, Korea. In: Proceedings of the 5th ACM SIGSPATIAL International Workshop on Mobile Geographic Information Systems. ACM, pp. 12–18.
- Zha, Y., Gao, J., Ni, S., 2003. Use of normalized difference built-up index in automatically mapping urban areas from TM imagery. *Int. J. Remote Sens.* 24 (3), 583–594.
- Zhang, G.J., Cai, M., Hu, A., 2013. Energy consumption and the unexplained winter warming over northern Asia and North America. *Nat. Clim. Chang.* 3 (5), 466.
- Zhao, C., Jensen, J., Weng, Q., Weaver, R., 2018. A geographically weighted regression analysis of the underlying factors related to the surface urban Heat Island phenomenon. *Remote Sens.* 10 (9), 1428.
- Zhao, H., Chen, X., 2005, July. Use of normalized difference bareness index in quickly mapping bare areas from TM/ETM+. In: International Geoscience and Remote Sensing Symposium, Vol. 3 (p. 1666).
- Zhou, W., Huang, G., Cadenasso, M.L., 2011. Does spatial configuration matter? Understanding the effects of land cover pattern on land surface temperature in urban landscapes. *Landscape Urban Plan.* 102 (1), 54–63.
- Zhou, W., Wang, J., Cadenasso, M.L., 2017. Effects of the spatial configuration of trees on urban heat mitigation: a comparative study. *Remote Sens. Environ.* 195, 1–12.
- Ziaul, S., Pal, S., 2018. Anthropogenic heat flux in English bazar town and its surroundings in West Bengal, India. *Remote Sens. Appl.: Soc. Environ.* 11, 151–160.
- Ziaul, S., Pal, S., 2019. Assessing outdoor thermal comfort of English Bazar Municipality and its surrounding, West Bengal, India. *Adv. Space Res.* 64 (3), 567–580.
- Ziaul, S., Pal, S., 2020. Modeling the effects of green alternative on heat island mitigation of a meso level town, West Bengal, India. *Adv. Space Res.* 65 (7), 1789–1802.
- Zipper, S.C., Schatz, J., Singh, A., Kucharik, C.J., Townsend, P.A., Loheide II, S.P., 2016. Urban heat island impacts on plant phenology: intra-urban variability and response to land cover. *Environ. Res. Lett.* 11 (5), 054023.